Modeling, Identification and Control of High-Speed ASVs: Theory and Experiments

Bjørn-Olav Holtung Eriksen, Morten Breivik

Abstract This paper considers a powerful approach to modeling, identification and control of high-speed autonomous surface vehicles (ASVs) operating in the displacement, semi-displacement and planing regions. The approach is successfully applied to an 8.45 m long ASV capable of speeds up to 18 m/s, resulting in a high-quality control-oriented model. The identified model is used to design four different controllers for the vessel speed and yaw rate, which have been tested through full-scale experiments in the Trondheimsfjord. The controllers are compared using various performance metrics, and two controllers utilizing a model-based feedforward term is shown to achieve outstanding performance.

1 Introduction

The development of autonomous vehicles is moving rapidly forward. The automotive industry is particularly leading this trend. At sea, there is also a great potential for such vehicles, which are typically referred to as autonomous surface vehicles (ASVs). The use of such vehicles have scientific, commercial and military applications, and can result in reduced costs, increased operational persistence and precision, widened weather window of operations, improved personnel safety, and more environmentally friendly operations. In [1], an early overview of unmanned surface vehicles is given, while a more recent survey is presented in [8].

In this paper, we focus on modeling and control of small, agile ASVs which can operate at high speeds with aggressive maneuvers. These vehicles typically cover the whole range of speed regions for a surface vehicle, namely the displacement, semi-displacement and planing regions. Hence, they are challenging to model and

Bjørn-Olav Holtung Eriksen and Morten Breivik
Centre for Autonomous Marine Operations and Systems, Department of Engineering Cybernetics, Norwegian University of Science and Technology (NTNU), Trondheim, Norway, e-mail: bjorn-olav.h.eriksen@ieee.org and morten.breivik@ieee.org

control, and it therefore becomes challenging to develop a robust and precise motion control system which allows the vehicles to utilize their full potential. Specifically, this paper revisits the modeling and control approach originally suggested in [4] and further developed and reported in [3]. The method represents a control-oriented modeling approach and underlines the importance of developing and using good feedforward terms in the control law. The high-quality performance of the resulting motion control system was validated through several full-scale experiments with ASVs in the Trondheimsfjord in 2008 and 2009, both for target tracking and formation control applications. In this paper, we further develop this approach and go into greater details concerning the modeling and identification procedure and results.

Full-scale identification experiments based on the suggested modeling approach are conducted with a dual-use (manned/unmanned) ASV named Telemetron, see Figure 1, which is owned and operated by the company Maritime Robotics. The resulting identified model is shown to be very precise and cover the entire operational envelope of the ASV. This model subsequently forms the basis for a detailed performance comparison between four qualitatively different controllers, which are implemented and experimentally tested to control the speed and yaw rate of the Telemetron ASV. In particular, the controllers are: A PI feedback (FB) controller; a pure model-based feedforward controller based on the identified model (FF); a controller which is a combination of model-based feedforward and PI feedback (FF-FB); and a controller using feedback signals in the model-based feedforward term in combination with PI feedback, which can be characterized as a feedback linearization (FBL) controller. Relevant performance metrics are defined and used to compare these controllers to determine which is most precise and energy efficient.

Other relevant work concerning a control-oriented modeling approach can be found in e.g. [11] and [10].

The rest of the paper is structured as follows: Chapter 2 presents the main characteristics of the control-oriented modeling approach. Chapter 3 describes the model identification in detail, from experimental design to parameter identification. Chapter 4 describes the four controllers which are considered in the paper, while Chapter 5 presents the results from the motion control experiments. Finally, Chapter 6 concludes the paper.

Fig. 1 The Telemetron ASV, which is a Polarcirkel Sport 8.45 m long dual-use ASV capable of speeds up to 18 m/s. Courtesy of Maritime Robotics.

2 2DOF control-oriented vessel model

The vast majority of surface vessel models are based on the 3DOF model [7]:

$$\dot{\boldsymbol{\eta}} = \boldsymbol{R}(\psi)\boldsymbol{\nu} \tag{1a}$$

$$\boldsymbol{M}\dot{\boldsymbol{\nu}} + \boldsymbol{C}_{RB}(\boldsymbol{\nu}) + \boldsymbol{C}_A(\boldsymbol{\nu}_r)\boldsymbol{\nu}_r + \boldsymbol{D}(\boldsymbol{\nu}_r)\boldsymbol{\nu}_r = \boldsymbol{\tau} + \boldsymbol{\tau}_{\text{wind}} + \boldsymbol{\tau}_{\text{wave}}, \tag{1b}$$

where $\boldsymbol{\eta} = \begin{bmatrix} N & E & \psi \end{bmatrix}^T \in \mathbb{R}^2 \times S^1$ is the vessel pose, $\boldsymbol{\nu} = \begin{bmatrix} u & v & r \end{bmatrix}^T \in \mathbb{R}^3$ is the vessel velocity and $\boldsymbol{\nu}_r$ denotes the relative velocity between the vessel and the water. The terms $\boldsymbol{\tau}, \boldsymbol{\tau}_{\text{wind}}, \boldsymbol{\tau}_{\text{wave}} \in \mathbb{R}^3$ represent the control input, wind and wave environmental disturbances, respectively. The matrix $\boldsymbol{R}(\psi)$ is the rotation matrix about the z-axis, the inertia matrix is $\boldsymbol{M} = \boldsymbol{M}_{RB} + \boldsymbol{M}_A$ where $\boldsymbol{M}_{RB}$ is the rigid-body mass and $\boldsymbol{M}_A$ is the added mass caused by the moving mass of water. The matrices $\boldsymbol{C}_{RB}(\boldsymbol{\nu})$ and $\boldsymbol{C}_A(\boldsymbol{\nu}_r)$ represent the rigid-body and hydrodynamic Coriolis and centripetal effects, respectively, while $\boldsymbol{D}(\boldsymbol{\nu}_r)$ captures the hydrodynamic damping of the vessel. An important limitation of (1b) is that it can be challenging to use for vessels operating outside of the displacement region. For approximating the operating region of a surface vessel, it is common to use the Froude number, defined as [6]:

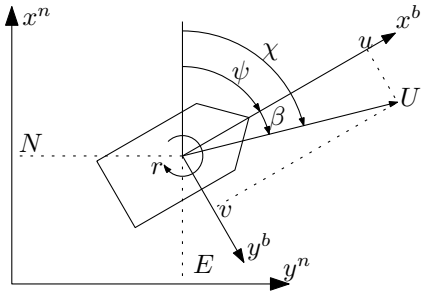

Fig. 2 Vessel variables. The superscripts $(\cdot)^n$ and $(\cdot)^b$ denote the NED and body-frames [7], respectively. The variables N, E and ψ are the vessel pose, u, v and r are the vessel velocity and U is the vessel speed over ground. The course χ is the sum of the heading ψ and the sideslip β.

$$Fn = \frac{U_r}{\sqrt{Lg}}, \tag{2}$$

where U_r is the vessel speed through water, L is the submerged vessel length and g is the acceleration of gravity. For Fn less than approximately 0.4, the hydrostatic pressure mainly carries the weight of the vessel, and we operate in the displacement region. When Fn is higher than 1.0 to 1.2, the hydrodynamic force mainly carries the weight of the vessel, and we operate in the planing region. For Fn between these values, we are in the semi-displacement region [6].

Typical ASVs have vessel lengths of up to 10 m, submerged length of up to 8 m and operating speeds up to 18 m/s. From Table 1, we see that an ASV with a submerged length of 8 m exits the displacement region already at 3.54 m/s, and enters the planing region at 8.86 m/s. Hence, (1b) is typically only suited for a small part of the ASV operating region, which motivates for an alternative model.

ASVs are generally underactuated, hence it it not possible to independently control surge, sway and yaw. We therefore choose to reduce the model to the 2DOF

Table 1: Operating speeds for displacement and planing regions. *Supply ships typically operate with speeds up to 7 m/s. It is therefore clear that supply ships generally operate in the displacement region.

Vessel type	**Submerged length**	**Maximum speed in displacement** ($Fn = 0.4$)	**Minimum speed in planing** ($Fn = 1.0$)
Small ASV	4 m	2.51 m/s	6.26 m/s
Large ASV	8 m	3.54 m/s	8.86 m/s
Small supply ship	50 m	8.86 m/s*	22.1 m/s*
Large supply ship	100 m	12.5 m/s*	31.3 m/s*

which we want to control, namely the speed over ground (SOG) $U = \sqrt{u^2 + v^2}$ and yaw rate (rate of turn, ROT). The kinematic equation (1a) is therefore modified to:

$$\begin{aligned} \dot{\boldsymbol{\eta}} &= \begin{bmatrix} \cos(\chi) & 0 \\ \sin(\chi) & 0 \\ 0 & 1 \end{bmatrix} \begin{bmatrix} U \\ r \end{bmatrix} \\ \dot{\chi} &= r + \dot{\beta}, \end{aligned} \tag{3}$$

where $\chi = \psi + \beta$ is the vessel course angle and β is the vessel sideslip. It should be noted that this model implies that:

- Since $U \geq 0$, we assume that the vessel is traveling forward, that is $u \geq 0$.
- The sideslip β enters the kinematic equation. For kinematic control (e.g. path following), this must be addressed by e.g. controlling course instead of heading.

To relax the limitation of operating in the displacement region implied by (1b), we propose a normalized non first-principles model. This is inspired by [4] and [3] where a steady-state model in a similar form is developed. Since the actual control input of the vessel is not forces, but rather motor throttle and rudder angle, we select these as inputs to the model. As a result, we also implicitly model the actuator dynamics. Let the motor throttle be given as $\tau_m \in [0,1]$ and the rudder input be given as $\tau_\delta \in [-1,1]$. Denoting the vessel velocity as $\boldsymbol{x} = \begin{bmatrix} U & r \end{bmatrix}^T \in \mathbb{R}^2$ and the control input as $\boldsymbol{\tau} = \begin{bmatrix} \tau_m & \tau_\delta \end{bmatrix}^T \in \mathbb{R}^2$, we propose the model:

$$\boldsymbol{M}(\boldsymbol{x})\dot{\boldsymbol{x}} + \boldsymbol{\sigma}(\boldsymbol{x}) = \boldsymbol{\tau}, \tag{4}$$

where the inertia matrix $\boldsymbol{M}(\boldsymbol{x}) = \text{diag}\left(m_U(\boldsymbol{x}), m_r(\boldsymbol{x})\right)$ is diagonal with elements of quantities $\left[\frac{1}{\text{m/s}^2} \; \frac{1}{1/\text{s}^2}\right]$, and $\boldsymbol{\sigma}(\boldsymbol{x}) = \begin{bmatrix} \sigma_U(\boldsymbol{x}) & \sigma_r(\boldsymbol{x}) \end{bmatrix}^T$ is a unit-less damping term. Notice that both are functions of $\boldsymbol{x}$, which allows for a nonlinear model. The reader should also note that centripetal effects are not explicitly included in (4) due to the choice of coordinates.

3 Model identification

Identifying the parameters of (4) require a series of experiments to be performed. In this section, we describe the identification experiments, parameterization of the inertia and damping terms, and the methodology used for parameter identification.

3.1 Vessel platform and hardware

As already mentioned, the vessel used in this work is the Telemetron ASV. It is a dual-use vessel for both manned and unmanned operations, and is equipped with a number of sensors and a proprietary control system. Some of the specifications are summarized in Table 2.

Table 2: Telemetron ASV specifications.

Component	**Description**
Vessel hull	Polarcirkel Sport 845
Length	8.45 m
Width	2.71 m
Weight	1675 kg
Propulsion system	Yamaha 225 HP outboard engine
Motor control	Electro-mechanical actuation of throttle valve
Rudder control	Hydraulic actuation of outboard engine angle with proportional-derivate (PD) feedback control
Navigation system	
Identification experiments	Kongsberg Seatex Seapath 330+
Control experiments	Hemisphere Vector VS330

3.2 Identification experiment design

Since we wish to identify damping and inertia terms, both steady-state and transient information is required. We therefore construct a series of step responses:

- Step changes in τ_m given a series of fixed rudder settings τ_δ, illustrated as orange trajectories in Figure 3.
- Step changes in τ_δ given a series of fixed throttle settings τ_m, illustrated as blue trajectories in Figure 3.

The steps are performed both for increasing and decreasing values to include the effect of hysteresis, and is designed to sample the U/r-space of the vessel as shown in Figure 3. It is assumed that the vessel response is symmetric in yaw, such that

it is sufficient to perform experiments only for positive rudder settings (which for the Telemetron ASV result in positive yaw rate). The vessel shall reach steady state between the step changes such that the damping terms can be identified from the steady-state response, while the inertia is identified from the transient response. The motor will be kept in forward gear throughout the entire experiment.

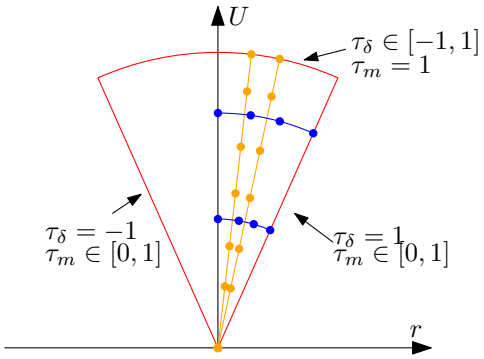

Fig. 3 Expected shape of the vessel velocity space, where the red line is the boundary of the velocity space. The orange and blue lines are examples of step change trajectories for fixed rudder and throttle, respectively. Note that only some trajectories are illustrated. The dots on the trajectories illustrate steady-state points.

The step changes in τ_m are performed as:

1. Start at $\tau_m = 0$. Select $\tau_\delta = 0$.
2. Step τ_m stepwise from 0 to 1 in steps of 0.1, letting the vessel SOG and ROT reach steady state before the next step is applied. Let the vessel do at least one full turn after reaching steady state, to be able to minimize the effect of external disturbances through averaging.
3. Step τ_m stepwise from 1 to 0, in the same fashion as in step 2.
4. Repeat step 2 and 3 with the next rudder setting.

Step changes in τ_δ are performed by interchanging τ_m and τ_δ. Identification experiments were carried out in the Trondheimsfjord 17$^{\text{th}}$ and 18$^{\text{th}}$ of December 2015.

3.3 Measurement extraction

To identify parameters for $\boldsymbol{M}(\boldsymbol{x})$ and $\boldsymbol{\sigma}(\boldsymbol{x})$, we need measurements of σ_U, σ_r, m_U and m_r for different vessel states $\boldsymbol{x}$.

3.3.1 Extraction of damping data

When the vessel is in steady state, the model (4) gives the relation:

$$\dot{\boldsymbol{x}} = \boldsymbol{0} \rightarrow \boldsymbol{\sigma}(\boldsymbol{x}) = \boldsymbol{\tau}, \tag{5}$$

hence measurements of the damping term can be taken simply as the control input when the vessel is at steady state. To reduce the influence of external forces, the

vessel state is averaged to extract measurements for σ_U and σ_r. This is shown for one of the fixed rudder settings in Figure 4. We observed that the motor response is greatly reduced for $\tau_m > 0.6$, hence measurements with $\tau_m > 0.6$ are omitted.

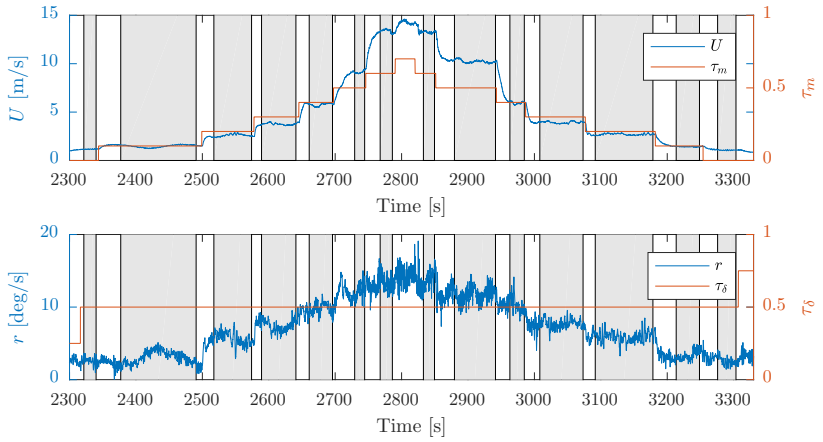

Fig. 4: Vessel response with a fixed rudder setting. The gray patches mark steady state regions.

By averaging the steady-state regions, we generate a set of N_σ measurements $\mathscr{D}_{\boldsymbol{\sigma}} = \{\{\boldsymbol{x}_1, \boldsymbol{x}_2, \ldots, \boldsymbol{x}_{N_\sigma}\}, \{\boldsymbol{\sigma}_1, \boldsymbol{\sigma}_2, \ldots, \boldsymbol{\sigma}_{N_\sigma}\}, \{\boldsymbol{\tau}_1, \boldsymbol{\tau}_2, \ldots, \boldsymbol{\tau}_{N_\sigma}\}\}$, which can be used for identifying parameters for the damping term. The damping measurements, with mirrored values for negative rudder settings, are shown in Figure 5.

3.3.2 Extraction of inertia data

To extract measurements for m_U and m_r, we have N_m step changes, and we create an estimate of the vessel response using N_m local first-order linear models. We approximate the SOG and ROT dynamics as SISO systems, hence for the i-th step, the linear approximation of the vessel SOG can be written as:

$$m_{U_i} \dot{\Delta U}_i + k_i \Delta U_i = \Delta \tau_{m_i}, \tag{6}$$

where the inertia m_{U_i} is assumed to be constant during the step, $k_i = \frac{\sigma_{U_i}^+ - \sigma_{U_i}^-}{U_i^+ - U_i^-}$, where $(\cdot)^-$ and $(\cdot)^+$ denotes the value prior to and after the step, is a linearized damping term, $\Delta U_i = U - U_i^-$ and $\Delta \tau_{m_i} = \tau_m - \tau_{m_i}^-$. The only unknown in (6) is the inertia m_{U_i}, hence we can find a suitable inertia m_{U_i} by simulating (6) for a set of possible inertias and selecting the inertia with the smallest squared estimation error, as shown in Figure 6. The measurement is taken as $(\boldsymbol{x}, m_U) = \left(\left(\frac{U_i^+ + U_i^-}{2}, \frac{r_i^+ + r_i^-}{2}\right), m_{U_i}\right)$. The same approach is employed for identifying inertia for ROT.

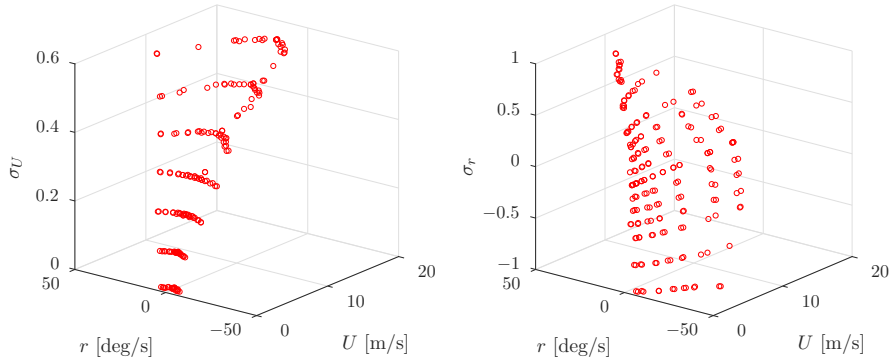

(a) σ_U measurements (b) σ_r measurements

Fig. 5: Damping term measurements from averaging of steady-state responses. Measurements for negative rudder settings are obtained by mirroring the data.

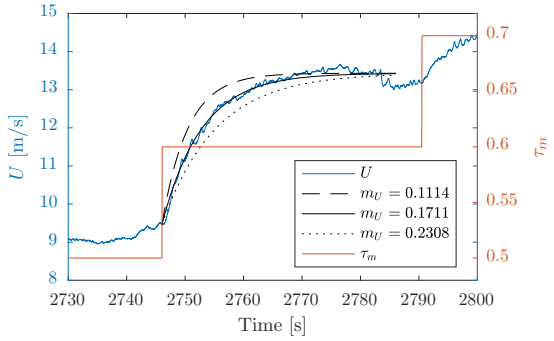

Fig. 6 Inertia measurement extraction for a step in the SOG. It is clear that $m_U = 0.1711$ is the best fit.

It should be noted that, in contrast to identifying damping, we obtain two sets of measurements $\mathscr{D}_{m_U} = \left\{\{\boldsymbol{x}_1, \boldsymbol{x}_2, \ldots, \boldsymbol{x}_{N_{m_U}}\}, \{m_{U_1}, m_{U_2}, \ldots, m_{U_{N_{m_U}}}\}\right\}$ and $\mathscr{D}_{m_r} = \left\{\{\boldsymbol{x}_1, \boldsymbol{x}_2, \ldots, \boldsymbol{x}_{N_{m_r}}\}, \{m_{r_1}, m_{r_2}, \ldots, m_{r_{N_{m_r}}}\}\right\}$ containing N_{m_U} and N_{m_r} measurements respectively. The inertia measurements are shown in Figure 7.

3.3.3 Data preprocessing

Before the measurements are used for parameter identification, some preprocessing is required:

- Damping measurements with $\tau_\delta = 0$ should result in zero yaw rate. Even though we average the steady-state response, some offset will be present. Hence, all

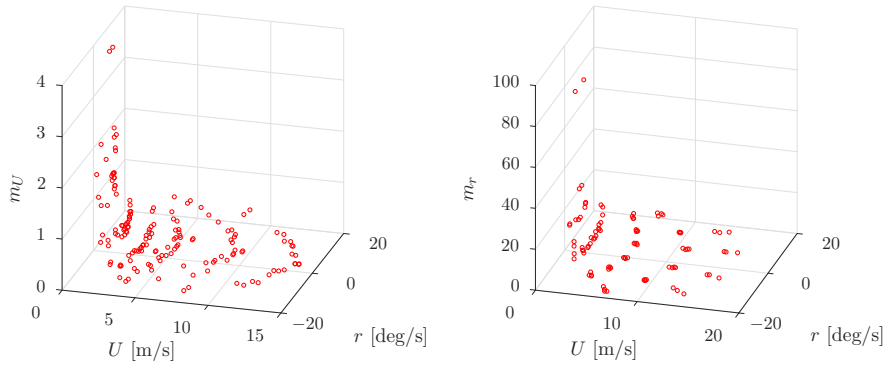

(a) m_U measurements (b) m_r measurements

Fig. 7: Inertia term measurements. Measurements for negative rudder settings are obtained by mirroring the data.

measurements $(U, r, \sigma_U, \sigma_r) \in \mathscr{D}_{\boldsymbol{\sigma}}$ with $\tau_\delta = \sigma_r = 0$ should be be modified as $(U, r, \sigma_U, \sigma_r) = (U, 0, \sigma_U, \sigma_r)$.

- Since the domains of U and r are different, the measurements should be normalized. We have applied zero-mean and unit variance normalization individually for each measurement set $\mathscr{D}_{\boldsymbol{\sigma}}, \mathscr{D}_{m_U}$ and $\mathscr{D}_{m_r}$.

3.4 Parameter identification

This section describes identification of the parameters of (4) based on the measurement sets $\mathscr{D}_{\boldsymbol{\sigma}}, \mathscr{D}_{m_U}$ and $\mathscr{D}_{m_r}$.

3.4.1 Linear regression

For identification of model parameters, we use linear regression [2]. This requires that the terms in (4) are linear in the parameters, e.g. that the damping and inertia terms can be written as:

$$\begin{aligned} \sigma_U(\boldsymbol{x}) &= \boldsymbol{\phi}_\sigma(\boldsymbol{x})^T \boldsymbol{\beta}_{\sigma_U}, \qquad & \sigma_r(\boldsymbol{x}) &= \boldsymbol{\phi}_\sigma(\boldsymbol{x})^T \boldsymbol{\beta}_{\sigma_r} \\ m_U(\boldsymbol{x}) &= \boldsymbol{\phi}_M(\boldsymbol{x})^T \boldsymbol{\beta}_{m_U}, \qquad & m_r(\boldsymbol{x}) &= \boldsymbol{\phi}_M(\boldsymbol{x})^T \boldsymbol{\beta}_{m_r}, \end{aligned} \tag{7}$$

where $\boldsymbol{\phi}_\sigma(\boldsymbol{x})$ and $\boldsymbol{\phi}_M(\boldsymbol{x})$ are vectors of basis functions (also called regressors) while $\boldsymbol{\beta}_{\sigma_U}, \boldsymbol{\beta}_{\sigma_r}, \boldsymbol{\beta}_{m_U}$ and $\boldsymbol{\beta}_{m_r}$ are parameter vectors. This generalizes as a function:

$$\hat{y} = \boldsymbol{\phi}(\boldsymbol{x})^T \boldsymbol{\beta}. \tag{8}$$

For the model (8), one can, given a data set $\{\{\boldsymbol{x}_1, \boldsymbol{x}_2, \ldots, \boldsymbol{x}_N\}, \{y_1, y_2, \ldots, y_N\}\}$ and a parameter vector $\boldsymbol{\beta}$, define the weighted square loss function:

$$\varepsilon = \frac{1}{N} \sum_{i=1}^{N} W_{ii} \left(y_i - \boldsymbol{\phi}(\boldsymbol{x}_i)^T \boldsymbol{\beta}\right)^2, \tag{9}$$

where W_{ii} is a weight for sample i. By defining $\boldsymbol{Y} = \begin{bmatrix} y_1 & y_2 & \ldots & y_N \end{bmatrix}^T$ and $\boldsymbol{X} = \begin{bmatrix} \boldsymbol{\phi}(\boldsymbol{x}_1)^T & \boldsymbol{\phi}(\boldsymbol{x}_2)^T & \ldots & \boldsymbol{\phi}(\boldsymbol{x}_N)^T \end{bmatrix}^T$ one can find the $\boldsymbol{\beta}$ that minimizes (9) as:

$$\boldsymbol{\beta} = (\boldsymbol{X}^T \boldsymbol{W} \boldsymbol{X})^{-1} \boldsymbol{X}^T \boldsymbol{W} \boldsymbol{Y}, \tag{10}$$

where $\boldsymbol{W} = \text{diag}(W_{11}, W_{22}, \ldots, W_{NN})$. This is known as weighted linear least-squares regression.

A well known issue with linear regression, especially with large parameter vectors, is the problem of overfitting. To reduce this problem, one can penalize large parameter values by adding a regularization term to (9) as:

$$\varepsilon = \frac{1}{N} \sum_{i=1}^{N} W_{ii} \left(y_i - \boldsymbol{\phi}(\boldsymbol{x}_i)^T \boldsymbol{\beta}\right)^2 + \lambda R(\boldsymbol{\beta}), \tag{11}$$

where $\lambda > 0$ is a regularization weight, and the choice of the regularization term $R(\boldsymbol{\beta})$ is problem dependent. We choose ℓ_1-regularization where $R(\boldsymbol{\beta}) = \|\boldsymbol{\beta}\|_1$, also known as lasso, which has the property of driving parameters to zero for sufficiently high values of λ [2]. This penalizes basis functions with low sensitivities to the loss function, and favors sparsity in the parameter vector.

It should be noted that introducing regularization provides one parameter more to the problem, in form of the regularization weight λ. Additionally, there exist no closed form solution to minimizing (11) with respect to $\boldsymbol{\beta}$. However, given a regularization parameter λ, the solution can be found through quadratic programming techniques.

3.4.2 Cross-validation (CV)

For identifying hyperparameters, such as the regularization weight λ, one can use cross-validation (CV). This involves dividing the available data into a training set and a validation set, where the training set is used for solving the parameter estimation while using the validation set for evaluating the loss. Hyperparameters can then be identified by minimizing the loss with respect to the hyperparameters. There exist different methods for dividing the available data, e.g. κ-fold, leave-p-out and leave-one-out (which is a special case of leave-p-out). Leave-one-out CV evaluates all possible combinations of leaving one sample for the validation set, hence for a data set of N samples this will result in N combinations of training and validation sets. We chose to use leave-one-out CV based on this property, while the limited data size ensures computational feasibility.

It should be noted that when performing both positive and negative step changes (see Figure 4), steady-state points with the same $\boldsymbol{\tau}$ will have quite similar (U, r)

coordinates. Hence, one should handle groups of measurements when dividing the measurements into training and validation data.

3.4.3 Damping term

From the structure of the damping measurements in Figure 5, we propose to use polynomial basis functions for the damping term in (4). This is also motivated by [7] where polynomial damping terms are used. The power of the polynomial is chosen as four, which is assumed to be sufficient to capture hydrodynamic damping and actuator dynamics. Hence, the regressor is defined as the 15-element vector:

$$\boldsymbol{\phi}_{\sigma}(\boldsymbol{x}) = \left[1,\, U,\, r,\, U^2,\, Ur,\, r^2,\, U^3,\, U^2 r,\, Ur^2,\, r^3,\, U^4,\, U^3 r,\, U^2 r^2,\, Ur^3,\, r^4\right]^T. \quad (12)$$

The parameter vectors $\boldsymbol{\beta}_{\sigma_U}$ and $\boldsymbol{\beta}_{\sigma_r}$ are identified by minimizing (11) with respect to $\boldsymbol{\beta}$. The regularization parameter is found as described in Section 3.4.2. A surface plot of the damping function is shown in Figure 8.

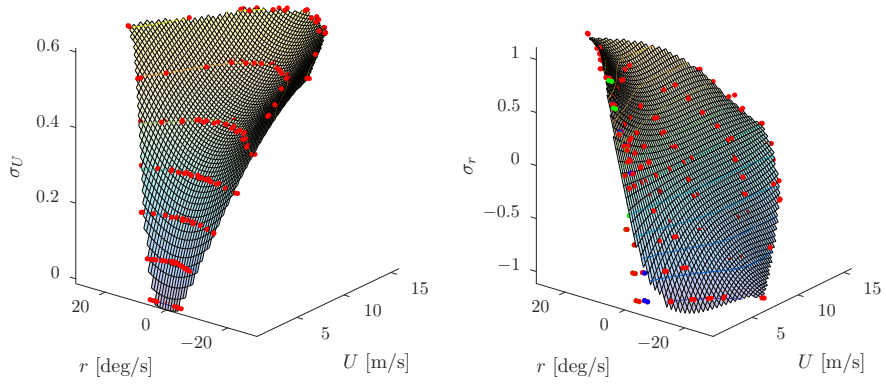

(a) $\sigma_U(\boldsymbol{x})$ (b) $\sigma_r(\boldsymbol{x})$

Fig. 8: Polynomial function for the damping term. The scatter points are the measuring points, where red points have weight $W = 1$, blue points have $W = 0.5$ and green points have $W = 0.1$.

3.4.4 Inertia term

From the structure of the inertia measurements in Figure 7, it is clear that a polynomial model will struggle to fit the data well. We therefore introduce an asymptotic

basis function $\tanh(a(U-b))$ in addition to the polynomial terms. The regressor for the inertia terms is hence defined as the 16-element vector:

$$\boldsymbol{\phi}_M(\boldsymbol{x}) = \big[1,\, U,\, r,\, U^2,\, Ur,\, r^2,\, U^3,\, U^2r,\, Ur^2,\, r^3,\, U^4,\, U^3r,\, U^2r^2,\, Ur^3,\, r^4,\, \tanh(a(U-b))\big]^T. \tag{13}$$

Notice that the asymptotic basis function introduces two more hyperparameters in the regression problem, namely a and b. To identify these hyperparameters, we again use leave-one-out CV, as described in Section 3.4.2. Notice that we use regularization when we identify these hyperparameters, individually of the linear regression. The motivation for this is that the position of the steep asymptote in the inertial measurement will move with changing ocean currents and external forces. Adding regularization when identifying the hyperparameters increases the robustness of the identified inertia term by adding a cost to choosing high parameter values for the asymptotic term and hence limiting the gradient of the asymptotic term.

The parameter vectors $\boldsymbol{\beta}_{m_U}, \boldsymbol{\beta}_{m_r}$ are, as for the damping term, identified by minimizing (11) with respect to $\boldsymbol{\beta}$. The hyperparameters are identified using CV. It should be noted that we use ℓ_1-regularization when identifying the hyperparameters (a_{m_U}, b_{m_U}) and (a_{m_r}, b_{m_r}).

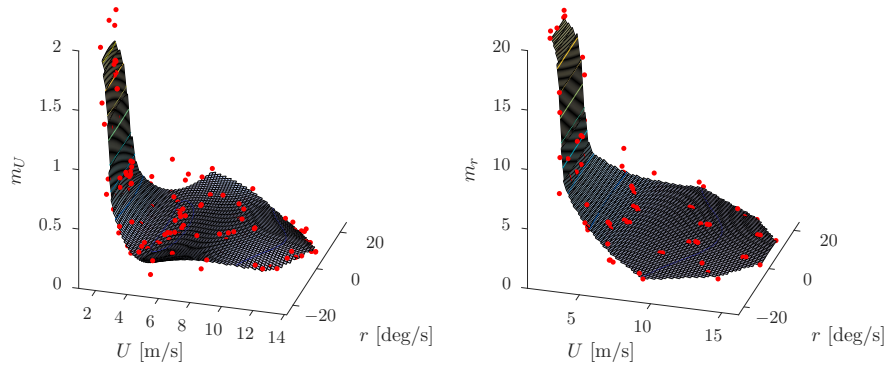

(a) $m_U(\boldsymbol{x})$ (b) $m_r(\boldsymbol{x})$

Fig. 9: Function for the inertia term. The scatter points are the measuring points.

3.5 Model verification

To qualitatively verify the identified vessel model, we simulate the model with the input sequence from an experiment not used in the model identification and compare

the results. The model (4), with damping and inertia parameterization and parameters as identified in Section 3.4, is simulated with the recorded input sequence to obtain the response shown in Figure 10. Based on the comparison, we see that the model captures the dynamics of the vessel, although with slight offsets especially for ROT. The simulated transient response coincides well with the real vessel response.

A design choice for the identification experiments was the assumed shape of the vessel operating space, discussed in Section 3.2 and illustrated in Figure 3. This design choice is verified by estimating the actual vessel operating space. This can be generated by using all the steady-state velocities obtained during the identification, as shown in Figure 11. By comparing the actual and assumed operating spaces, we see that the shapes are very similar.

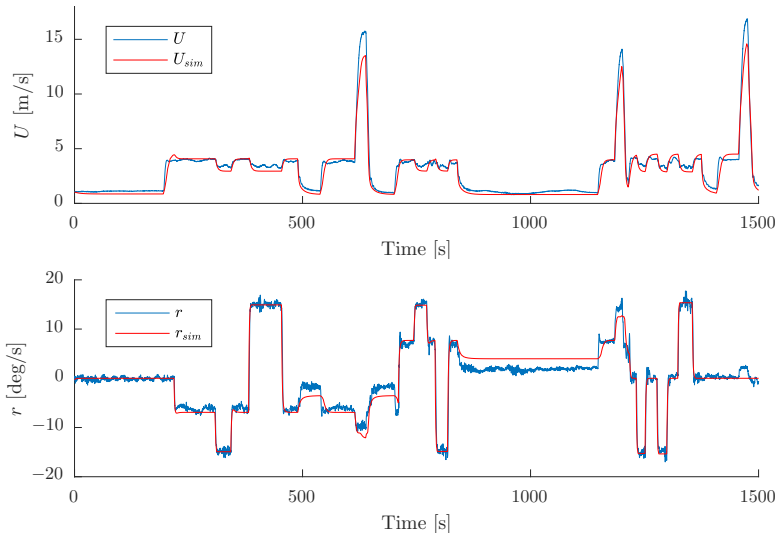

Fig. 10: Real and simulated vessel response. The deviation at high SOG is caused by exiting the valid domain of the identified model.

Fig. 11 Identified steady-state velocities. The red boundary line is estimated by least-squares curve fitting a fourth order polynomial. Note that that $U < 0.75$ m/s is not part of the vessel operating space as ocean current lower-bound the SOG.

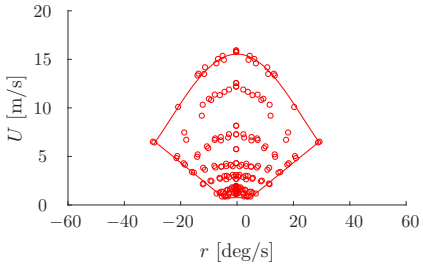

4 Controller design

In this section, we design four controllers to be compared through experiments:
1. A proportional-integral feedback (FB) controller.
2. A feedforward (FF) controller.
3. A combined feedforward and feedback (FF-FB) controller.
4. A feedback-linearizing (FBL) controller.

4.1 Controller types

This section describes the controller formulations, and the resulting closed-loop dynamics.

4.1.1 Model uncertainties

The model (4) does not account for modeling uncertainties. For closed-loop analysis, we therefore add an unknown bias term and modify the model as:

$$\boldsymbol{M}(\boldsymbol{x})\dot{\boldsymbol{x}} + \boldsymbol{\sigma}(\boldsymbol{x}) = \boldsymbol{\tau} + \boldsymbol{b}, \tag{14}$$

where $\boldsymbol{b}$ is assumed to be slowly varying, hence $\dot{\boldsymbol{b}} \approx \boldsymbol{0}$.

4.1.2 Proportional-integral feedback (FB) controller

The FB controller is a proportional-integral controller with gain scheduling of the proportional gain using the inertia term of the identified model (4):

$$\boldsymbol{\tau}_{FB} = -\boldsymbol{M}(\boldsymbol{x})\boldsymbol{K}_p\tilde{\boldsymbol{x}} - \boldsymbol{K}_i \int_{t_0}^{t} \tilde{\boldsymbol{x}}(\gamma)\mathrm{d}\gamma, \tag{15}$$

where $\boldsymbol{K}_p > 0$ is a diagonal proportional gain matrix, $\boldsymbol{K}_i > 0$ is a diagonal integral gain matrix and $\tilde{\boldsymbol{x}} = \boldsymbol{x} - \boldsymbol{x}_d$. By inserting (15) into (14) we derive the error dynamics:

$$\dot{\tilde{\boldsymbol{x}}} = -\boldsymbol{K}_p\tilde{\boldsymbol{x}} + \boldsymbol{M}(\boldsymbol{x})^{-1}\left(\boldsymbol{b} - \boldsymbol{\sigma}(\boldsymbol{x}) - \boldsymbol{K}_i \int_{t_0}^{t} \tilde{\boldsymbol{x}}(\gamma)\mathrm{d}\gamma\right) + \dot{\boldsymbol{x}}_d, \tag{16}$$

where we see that the integrator must compensate for modeling errors and damping. Even if $\boldsymbol{K}_i \int_{t_0}^{t} \tilde{\boldsymbol{x}}(\gamma)\mathrm{d}\gamma = \boldsymbol{b} - \boldsymbol{\sigma}(\boldsymbol{x})$ and $\tilde{\boldsymbol{x}} = \boldsymbol{0}$, we will still not be able to track a changing reference since $\boldsymbol{\sigma}(\boldsymbol{x})$ is changing with $\boldsymbol{x}$, and $\dot{\boldsymbol{x}}_d \neq \boldsymbol{0}$ for a changing reference.

4.1.3 Feedforward (FF) controller

The model-based FF controller feedforwards the desired acceleration and velocity:

$$\boldsymbol{\tau}_{FF} = \boldsymbol{M}(\boldsymbol{x})\dot{\boldsymbol{x}}_d + \boldsymbol{\sigma}(\boldsymbol{x}_d). \tag{17}$$

Notice that we use the measured state $\boldsymbol{x}$ when computing the inertia term, and the desired state $\boldsymbol{x}_d$ when computing the damping term. The error dynamics becomes:

$$\dot{\tilde{\boldsymbol{x}}} = \boldsymbol{M}(\boldsymbol{x})^{-1}\left(\boldsymbol{\sigma}(\boldsymbol{x}_d) - \boldsymbol{\sigma}(\boldsymbol{x}) + \boldsymbol{b}\right), \tag{18}$$

which has an equilibrium $\boldsymbol{x} = \boldsymbol{\sigma}^{-1}(\boldsymbol{\sigma}(\boldsymbol{x}_d) + \boldsymbol{b})$, given that $\boldsymbol{\sigma}^{-1}(\cdot)$ is well-defined. Hence, if $\boldsymbol{b} \neq \boldsymbol{0}$ we will have some tracking and steady-state offset.

4.1.4 Combined feedforward and feedback (FF-FB) controller

The FF-FB controller combines the FF and FB controllers as:

$$\boldsymbol{\tau}_{FF\text{-}FB} = \boldsymbol{M}(\boldsymbol{x})\dot{\boldsymbol{x}}_d + \boldsymbol{\sigma}(\boldsymbol{x}_d) - \boldsymbol{M}(\boldsymbol{x})\boldsymbol{K}_p\tilde{\boldsymbol{x}} - \boldsymbol{K}_i\int_{t_0}^{t}\tilde{\boldsymbol{x}}(\gamma)\mathrm{d}\gamma. \tag{19}$$

Inserting (19) into (14), we can derive the error dynamics:

$$\dot{\tilde{\boldsymbol{x}}} = -\boldsymbol{K}_p\tilde{\boldsymbol{x}} + \boldsymbol{M}(\boldsymbol{x})^{-1}\left(\boldsymbol{\sigma}(\boldsymbol{x}_d) - \boldsymbol{\sigma}(\boldsymbol{x}) + \boldsymbol{b} - \boldsymbol{K}_i\int_{t_0}^{t}\tilde{\boldsymbol{x}}(\gamma)\mathrm{d}\gamma\right), \tag{20}$$

where one should notice that if the $\boldsymbol{\sigma}(\boldsymbol{x}_d)$ would be substituted with $\boldsymbol{\sigma}(\boldsymbol{x})$ we would have a feedback-linearizing controller. The motivation for using $\boldsymbol{\sigma}(\boldsymbol{x}_d)$ in (17) is to increase the robustness and introduce an extra "driving" term in addition to the proportional feedback driving the error to zero.

4.1.5 Feedback-linearizing (FBL) controller

The FBL controller is similar to (19), but computes the damping term for the measured velocity:

$$\boldsymbol{\tau}_{FBL} = \boldsymbol{M}(\boldsymbol{x})\dot{\boldsymbol{x}}_d + \boldsymbol{\sigma}(\boldsymbol{x}) - \boldsymbol{M}(\boldsymbol{x})\boldsymbol{K}_p\tilde{\boldsymbol{x}} - \boldsymbol{K}_i\int_{t_0}^{t}\tilde{\boldsymbol{x}}(\gamma)\mathrm{d}\gamma, \tag{21}$$

which can cause poor robustness with respect to disturbances and time delays in the control system. The FBL controller is often used for analysis of closed-loop systems due to the simple error dynamics:

$$\dot{\tilde{\boldsymbol{x}}} = -\boldsymbol{K}_p\tilde{\boldsymbol{x}} + \boldsymbol{M}(\boldsymbol{x})^{-1}\left(\boldsymbol{b} - \boldsymbol{K}_i\int_{t_0}^{t}\tilde{\boldsymbol{x}}(\gamma)\mathrm{d}\gamma\right). \tag{22}$$

4.2 Control architecture

The FB, FF and FF-FB controllers in Section 4.1 are realized by enabling the feedback, feedforward and both functions shown in Figure 12, respectively. The FBL controller is realized by combining the feedback and feedforward functions, while computing the feedforward damping as $\boldsymbol{\sigma}(\boldsymbol{x})$ instead of $\boldsymbol{\sigma}(\boldsymbol{x}_d)$.

To increase robustness in the implementation, saturation elements are placed at each output except for the proportional feedback element.

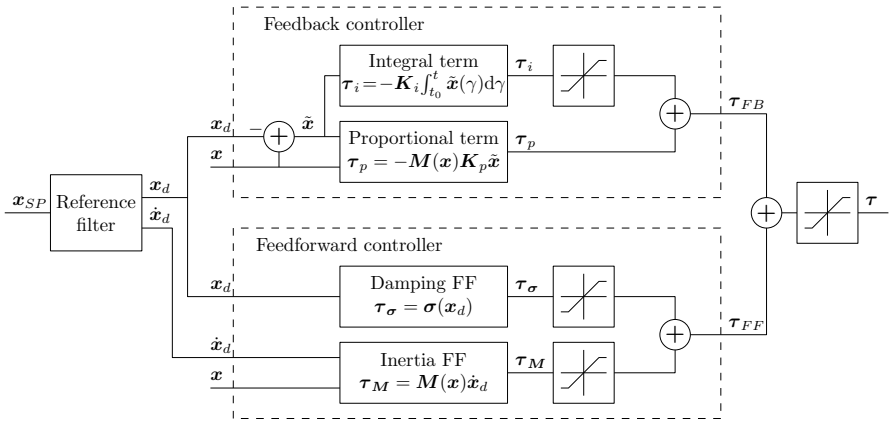

Fig. 12: Control architecture. The different controllers are realized through combinations of the feedback and feedforward functions.

To ensure continuous reference signals $\boldsymbol{x}_d$ and $\dot{\boldsymbol{x}}_d$, we employ a second-order reference filter from a possibly discontinuous, user-specified setpoint signal $\boldsymbol{x}_{SP}$. Additionally, we limit the acceleration such that the reference signals are feasible with respect to the vessel capability. The filter is parameterized as [7]:

$$\begin{bmatrix} \dot{\boldsymbol{x}}_d \\ \ddot{\boldsymbol{x}}_d \end{bmatrix} = \begin{bmatrix} \boldsymbol{0} & \boldsymbol{I} \\ -\boldsymbol{\Omega}^2 & -2\boldsymbol{\Delta}\boldsymbol{\Omega} \end{bmatrix} \begin{bmatrix} \boldsymbol{x}_d \\ \dot{\boldsymbol{x}}_d \end{bmatrix} + \begin{bmatrix} \boldsymbol{0} \\ \boldsymbol{\Omega}^2 \end{bmatrix} \boldsymbol{x}_{SP} \tag{23}$$

while imposing the acceleration limits:

$$\dot{U}_d \in \left[\dot{U}_{d_{\min}}, \dot{U}_{d_{\max}}\right], \quad \dot{r}_d \in \left[\dot{r}_{d_{\min}}, \dot{r}_{d_{\max}}\right]. \tag{24}$$

The relative damping ratio matrix $\boldsymbol{\Delta} > 0$ is chosen as identity to achieve a critically damped system, while the diagonal natural frequency matrix $\boldsymbol{\Omega} > 0$ is a tuning parameter.

5 Motion control experiments

To evaluate the performance of the controllers described in Section 4.1, they were implemented on the Telemetron ASV and tested in the Trondheimsfjord on the 13$^{\text{th}}$ and 14$^{\text{th}}$ of October 2016. During the first day, the sea state can be characterized as calm, which refer to significant wave heights of 0–0.1 m, while the sea state for the second day can be characterized as slight, which refer to significant wave heights of 0.5–1.25 m [9]. In total, three different scenarios were tested in different sea states.

It should be noted that the time between the model identification and motion control experiments was about 10 months. The top speed of the vessel was reduced from 18 m/s to about 16 m/s, probably caused by algae growth on the hull.

5.1 Tuning parameters

The reference filter was tuned with a natural frequency of $\boldsymbol{\Omega} = \text{diag}(0.4, 1)$ and acceleration constraints $\dot{U}_{\max} = 0.75$ m/s^2, $\dot{U}_{\min} = -0.75$ m/s^2, $\dot{r}_{\max} = 0.1$ rad/s^2 and $\dot{r}_{\min} = -0.1$ rad/s^2. The feedback tuning parameters were selected as shown in Table 3. Unfortunately, an implementation error resulted in a too high integrator gain for the yaw rate feedback controller during the experiments in calm seas.

Table 3: Feedback tuning parameters.

Parameters	**Values**		
	FB	FF-FB	FBL
Sea state - Calm:			
$\boldsymbol{K}_p$	diag(0.15, 0.75)	diag(0.15, 0.75)	diag(0.15, 0.75)
$\boldsymbol{K}_i$	diag(0.015, 0.5)	diag(0.015, 0.5)	diag(0.015, 0.5)
Sea state - Slight:			
$\boldsymbol{K}_p$	diag(0.15, 1)	diag(0.1, 0.5)	diag(0.1, 0.5)
$\boldsymbol{K}_i$	diag(0.01, 0.25)	diag(0.0067, 0.125)	diag(0.0067, 0.125)

5.2 Performance metrics

To compare controller performance, it is beneficial to define suitable performance metrics. To simplify the analysis, it is also beneficial to combine the control inputs and outputs to one input and one output when calculating the metrics. Since the outputs have different units, we define the normalized signals $\bar{U}, \bar{U}_d, \bar{r}$ and $\bar{r}_d$ that are in the interval $[0, 1]$ in the expected operation space of the vessel. A combined error and control input can then be computed as:

$$\bar{e}(t) = \sqrt{(\bar{U}(t) - \bar{U}_d(t))^2 + (\bar{r}(t) - \bar{r}_d(t))^2}, \quad \bar{\tau}(t) = \sqrt{\tau_m^2 + \tau_\delta^2}. \tag{25}$$

Given these signals, we can define the integral of absolute error (IAE):

$$IAE(t) = \int_{t_0}^{t} |\bar{e}(\gamma)| \mathrm{d}\gamma, \tag{26}$$

which penalizes the error linearly with the magnitude and serves as a measure of control precision. A similar metric is the integral of square error (ISE), which penalizes large errors more than small errors.

The integral of absolute differentiated control (IADC) has been used earlier in a combined performance metric in [13], and is defined as:

$$IADC(t) = \int_{t_0}^{t} |\dot{\bar{\tau}}(\gamma)| \mathrm{d}\gamma, \tag{27}$$

which penalizes actuator changes and serves as a measure of actuator wear and tear.

The integral of absolute error times the integral of absolute differentiated control (IAE-ADC) is a combination of IAE and IADC:

$$IAE\text{-}ADC(t) = \int_{t_0}^{t} |\bar{e}(\gamma)| \mathrm{d}\gamma \int_{t_0}^{t} |\dot{\bar{\tau}}(\gamma)| \mathrm{d}\gamma, \tag{28}$$

which serves as a measure of control precision versus wear and tear.

The integral of absolute error times work (IAEW) scales IAE with energy consumption [12]:

$$IAEW(t) = \int_{t_0}^{t} |\bar{e}(\gamma)| \mathrm{d}\gamma \int_{t_0}^{t} P(\gamma) \mathrm{d}\gamma, \tag{29}$$

where $P(t)$ is the mechanical power applied by the engine. IAEW measures control precision versus energy consumption, hence it quantifies the energy efficiency. It is common to model the applied propeller force F as proportional to the square of the propeller speed, hence, $F \propto |n|n$ [7]. The mechanical energy can then be written as:

$$P(t) \propto U(t)|n(t)|n(t). \tag{30}$$

Since we use the metric in a relative comparison, we do not care about any scaling constant and set $P(t) = U(t)|n(t)|n(t)$.

5.3 Experiments in slight seas

All the scenarios were tested in slight seas, and here we present two of the scenarios.

5.3.1 Test 1 - High-speed trajectory tracking with steady states

The first test was intended to test a large portion of the vessel operating space while measuring both steady-state and transient performance. The test is symmetric in U_d and anti-symmetric in r_d. The vessel response in slight seas is shown in Figure 13.

Immediately, we observe that the FBL controller suffers from instability, caused by the feedback term $\boldsymbol{\sigma}(\boldsymbol{x})$ in (21). The oscillatory vessel state causes a dropout of the navigation system, stopping the experiment at $t \approx 194$ s. In general, using sensor measurements in model-based feedforward terms reduces the robustness with respect to time delays, sensor dropouts and noise. Using the reference in the feedforward terms avoids these problems. The FBL controller is not used in the other tests. The FF controller achieves good tracking, but naturally with some steady-state offset. The FB controller achieves poor tracking, while also being largely influenced by disturbances. The FF-FB controller has similar (or better) tracking performance than the FF controller while avoiding steady-state offsets, and at the same time better disturbance rejection than the FB controller. The FF, FF-FB and FBL controllers fail in tracking the first transient due to the control system time delay which causes problems with capturing the steep transient in the inertia term. It might be beneficial to limit the gradient $\nabla_{\boldsymbol{x}} \boldsymbol{M}(\boldsymbol{x})$ or saturating the inertia $\boldsymbol{M}(\boldsymbol{x})$ to avoid this behavior.

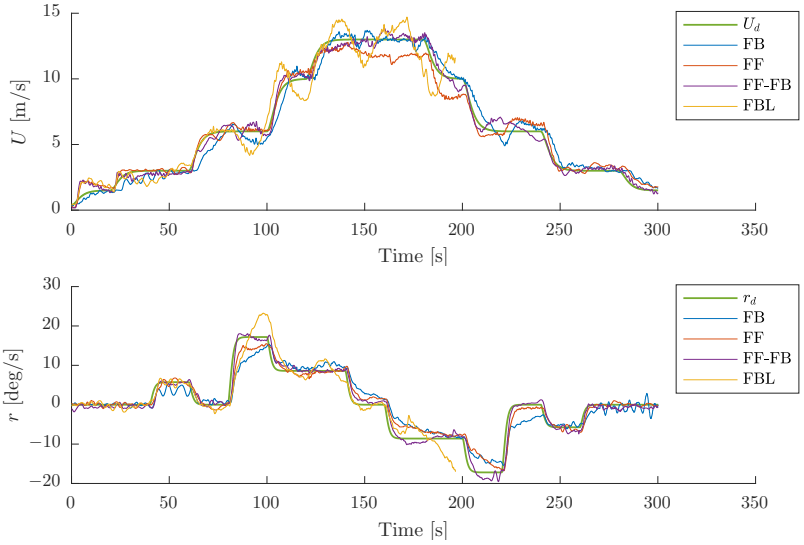

Fig. 13: Test 1 - High-speed trajectory tracking with steady states in slight seas. The feedback linearizing (FBL) controller fails at $t \approx 194$ s due to sensor dropout.

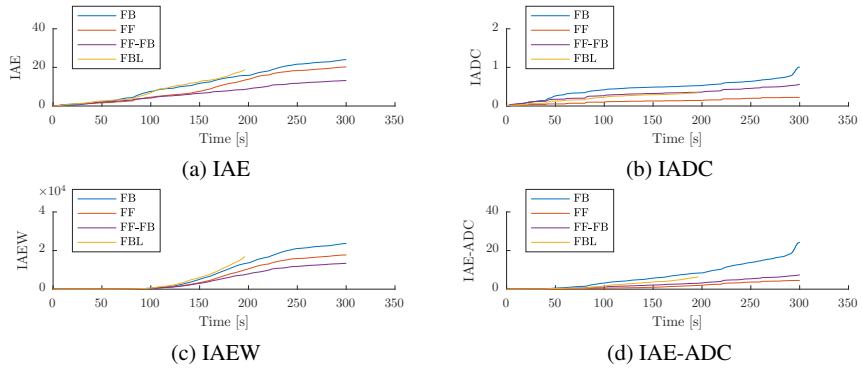

(a) IAE (b) IADC

(c) IAEW (d) IAE-ADC

Fig. 14: Performance metrics for Test 1 in slight seas.

The IAE (Figure 14a) shows that the FF-FB controller has the best control precision, while the FF controller is somewhat better than the FB and FBL controllers. From the IADC (Figure 14b), it is clear that the FB controller is tough on the actuators, while the FBL and FF-FB controllers are comparable. The FF controller is, as expected, the best with respect to wear and tear. From the IAEW (Figure 14c), the FF-FB controller has the best energy efficiency, the FF controller is second best and the FB controller places third. The FBL controller has a bad IAEW due to the oscillatory behavior. The IAE-ADC (Figure 14d) shows the same tendencies as the

IADC, but the FF-FB controller performs better than the FBL controller, and the gap between the FF-FB and FF controllers is smaller.

5.3.2 Test 2 - High-speed trajectory tracking without steady states

The second test was intended to investigate the tracking performance of the controllers. The reference is constantly changing without reaching steady state, and both moderate and high velocities are tested. This test was performed only in slight seas. From Figure 15, we observe that the FB controller again suffers from poor

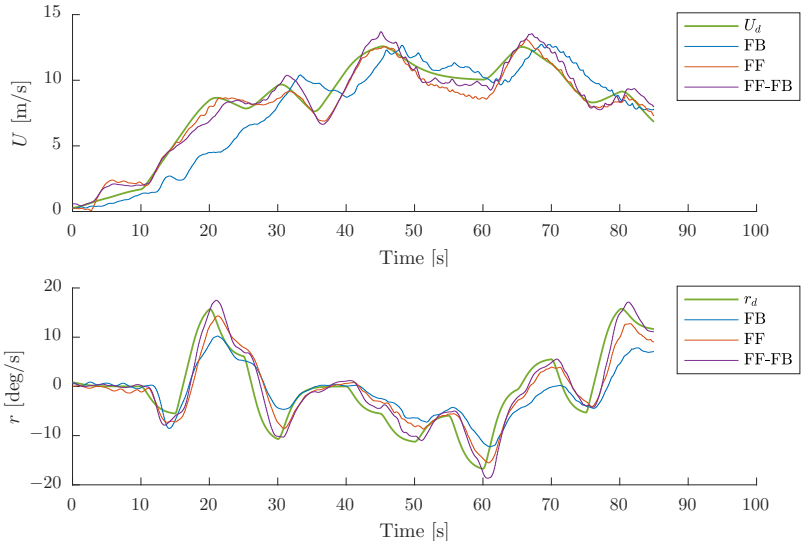

Fig. 15: Test 2 - High speed trajectory tracking without steady states in slight seas. The FF and FF-FB controllers far outperform the FB controller.

tracking and largely fails this test. The FF controller performs remarkably well and, from the time plot, the FF and FF-FB controllers seem to have equal performance.

From the performance metrics in Figure 16, the FB controller has the lowest performance, while the FF and FF-FB controllers are quite equal. The FF-FB controller has slightly better control precision (IAE) than the FF controller, at the cost of increased actuator wear and tear (IADC and IAE-ADC).

5.4 Experiments in calm seas

Two of the scenarios were tested in calm seas, and here we present one of them.

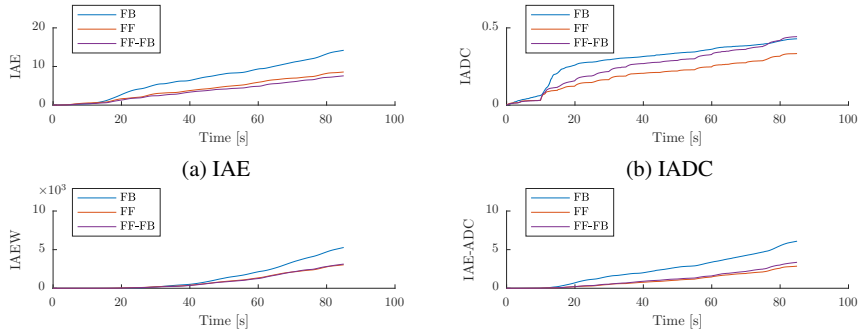

(a) IAE (b) IADC

(c) IAEW (d) IAE-ADC

Fig. 16: Performance metrics for Test 2 in slight seas.

5.4.1 Test 3 - Lower-speed trajectory tracking with steady states

The third test was intended to test lower velocities, especially for the yaw rate. The vessel response in calm seas is shown in Figure 17. Note that the integral gain for the yaw rate controller unfortunately was set too high by accident, causing oscillation in the yaw rate.

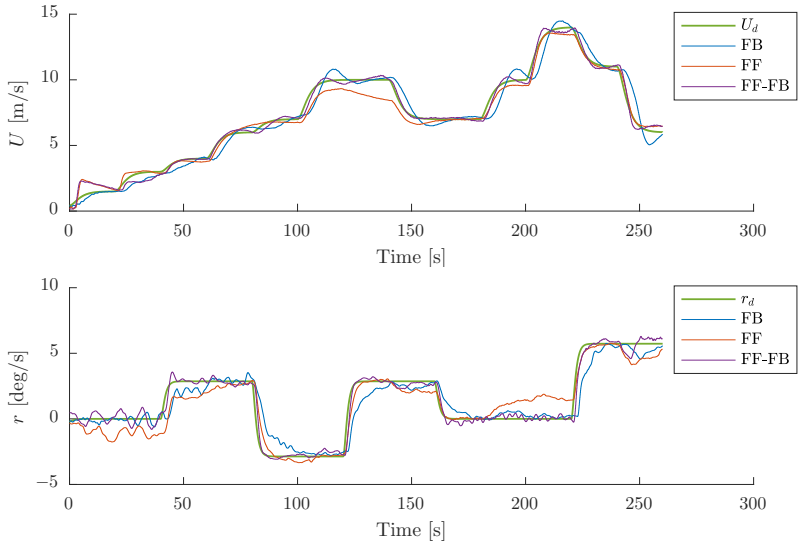

Fig. 17: Test 3 - Lower-speed trajectory tracking with steady states in calm seas. Observe the low amount of noise in the SOG-response compared to Figure 13.

From Figure 17, we observe that the FB controller again suffers from poor tracking, and struggles with steady-state offset in yaw rate (despite the high integrator gain). The FF controller also struggles with steady-state offset, but has superior performance in the transients. The FF-FB controller combines the performance of the FB and FF controllers and provides good tracking and low steady-state offset.

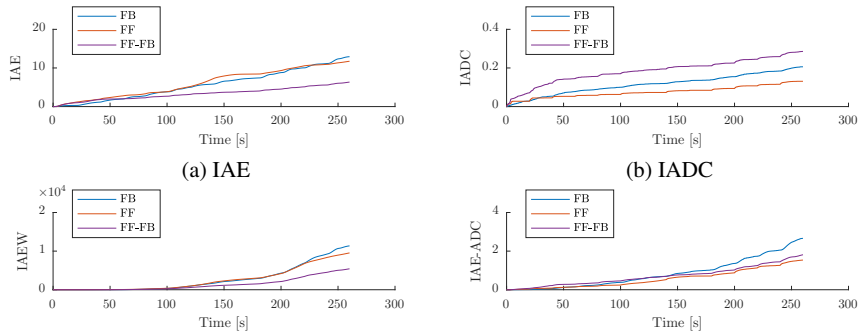

(a) IAE (b) IADC

(c) IAEW (d) IAE-ADC

Fig. 18: Performance metrics for Test 3 in calm seas.

From the performance metrics in Figure 18, we can draw the same conclusions as for Test 1. However, concerning the IADC, the FF-FB controller has the most wear and tear, which is probably caused by the initial oscillatory behavior in yaw rate due to the high integrator gain resulting in high initial condition sensitivity.

5.5 Motion control experiments summary

For controller evaluation, it is useful to compare the performance metrics. The final performance metric values for all the tests are presented in Table 4. We observe that:

- The FF and FF-FB controllers have the best performance:
  - The FF controller is best with respect to actuator wear and tear (IADC), also when scaled with the control precision (IAE-ADC).
  - The FF-FB controller is best with respect to control precision (IAE). In all tests except Test 2, it also has the best energy efficiency (IAEW). For Test 2, the FF and FF-FB controllers have near identical energy efficiency.
- The FF-FB controller has the most consistent control precision performance (IAE) for varying environmental conditions.
- The FF and FF-FB controllers have quite similar consistency of energy efficiency (IAEW) for varying environmental conditions.
- The FB controller has the worst metrics in all the tests, except for IADC in Test 2.

Table 4: The performance metrics are normalized for each test, and the controller performing best for each metric in each test is highlighted in bold. C/S refer to calm (C) and slight (S) seas. *For Test 1 in slight seas, the FBL controller did not complete the entire test, hence the S metrics of FBL Test 1 are not comparable.

Test case	**Controller**	**IAE**	**IADC**	**IAE-ADC**	**IAEW**
Test 1	FB	85.8 / 100.0	41.0 / 100.0	35.2 / 100.0	85.6 / 100.0
C/S	FF	71.1 / 84.2	**21.0** / **22.1**	**14.9** / **18.6**	65.6 / 74.9
	FF-FB	**41.5** / **54.9**	55.1 / 55.4	22.9 / 30.5	**42.0** / **56.5**
	FBL*	84.9 / 78.3	45.7 / 33.9	38.8 / 26.5	87.2 / 71.5
Test 2	FB	100.0	96.9	100.0	100.0
S	FF	60.4	**75.3**	**46.9**	**57.5**
	FF-FB	**53.4**	100.0	55.1	59.3
Test 3	FB	88.9 / 100.0	45.2 / 100.0	40.2 / 100.0	89.7 / 100.0
C/S	FF	80.8 / 97.5	**28.7** / **26.4**	**23.2** / **25.8**	75.3 / 83.1
	FF-FB	**43.7** / **45.2**	62.7 / 70.2	27.4 / 31.7	**42.8** / **45.1**

6 Conclusion

In this paper, we have presented a powerful approach to modeling, identification and control of high-speed ASVs operating in the displacement, semi-displacement and planing regions. We have used this approach on a high-speed ASV to successfully identify a control-oriented model of the vessel covering all its operating regions. Furthermore, we have through full-scale motion control experiments compared the performance of four controllers all utilizing the identified model:

- A proportional-integral feedback (FB) controller with gain scheduling.
- A feedforward (FF) controller.
- A combined feedforward and feedback (FF-FB) controller.
- A feedback-linearizing (FBL) controller.

By both qualitative and quantitative comparisons, it is shown that the FF-FB and FF controllers have superior performance over the two others. The FF-FB and FBL controllers are formulated almost identically, but the FF-FB controller has superior robustness and performance over the FBL controller.

From the results, we observe that model-based feedforward control is a powerful tool, which when used correctly will result in outstanding performance. There are, however, pitfalls reducing the robustness with respect to time delays, sensor dropouts and noise. This is the case for the FBL controller, where using the measured vessel velocity in the damping feedforward term causes instability.

Possibilities for further work include:

- Use the SOG and ROT controllers for closed-loop pose control for e.g. path following and target tracking scenarios.
- Use the SOG and ROT controllers and the identified model in combination with the dynamic window algorithm to achieve collision avoidance functionality, continuing the work in [5].

- Use the SOG and ROT controllers for manual velocity control through a joystick.
- Use the modeling approach for automatic and/or recursive model identification.
- Use the identified model to online modify the reference filter acceleration limits.

Acknowledgments

This work was supported by the Research Council of Norway through project number 244116, and through the Centres of Excellence funding scheme with project number 223254. The authors would like to express great gratitude to Maritime Robotics for placing the Telemetron ASV at our disposal, and especially Thomas Ingebretsen for help with implementing the controllers and supporting the experiments. The authors would also like to thank Andreas L. Flåten for valuable discussions on the topic of linear regression and cross-validation.

References

1. Bertram, V. (2008). Unmanned Surface Vehicles - A Survey. Skibsteknisk Selskab, Copenhagen, Denmark
2. Bishop C (2006) Pattern Recognition and Machine Learning. Springer Science + Business Media
3. Breivik M (2010) Topics in Guided Motion Control of Marine Vehicles. PhD thesis, Norwegian University of Science and Technology, Trondheim, Norway
4. Breivik M, Hovstein V E, Fossen T I (2008) Straight-Line Target Tracking for Unmanned Surface Vehicles. Model. Ident. Control. 29:131–149
5. Eriksen B-O H, Breivik M, Pettersen K Y, Wiig M S (2016) A Modified Dynamic Window Algorithm for Horizontal Collision Avoidance for AUVs. Proc. of IEEE CCA. Buenos Aires, Argentina
6. Faltinsen O M (2005) Hydrodynamics of High-Speed Marine Vehicles. Cambridge University Press
7. Fossen T I (2011) Handbook of Marine Craft Hydrodynamics and Motion Control. John Wiley & Sons Ltd
8. Liu Z, Zhang Y, Yu X, Yuan C (2016) Unmanned surface vehicles: An overview of developments and challenges. Annu Rev Control. 41:71–93
9. Prince W G, Bishop R E D (1974) Probabilistic Theory of Ship Dynamics. Chapman and Hall
10. Sonnenburg C R, Woolsey C A (2013) Modeling, Identification, and Control of an Unmanned Surface Vehicle. Journal of Field Robotics. 30(3):371–398.
11. Sonnenburg C R, Gadre A, Horner D, Kragelund S, Marcus A, Stilwell D J Woolsey C A (2010) Control-Oriented Planar Motion Modeling of Unmanned Surface Vehicles. Proc. of OCEANS 2010. Seattle, USA
12. Sørensen M E N, Breivik M (2015) Comparing Nonlinear Adaptive Motion Controllers for Marine Surface Vessels. Proc. of 10th IFAC MCMC. Copenhagen, Denmark
13. Sørensen M E N, Bjørne E S, Breivik M (2016) Performance Comparison of Backstepping-based Adaptive Controllers for Marine Surface Vessels. Proc. of IEEE CCA. Buenos Aires, Argentina